Published in final edited form as:
Acta Biomater. 2012 September ; 8(9): 3360–3371. doi:10.1016/j.actbio.2012.04.039.

Continuum modeling of neuronal cell under blast loading

Antoine Jérusalem[1] and
IMDEA Materials Institute, C/ Profesor Aranguren s/n, 28040 Madrid, Spain

Ming Dao[1]
Massachusetts Institute of Technology, 77 Massachusetts Avenue, Cambridge, MA 02139, USA

Abstract

Traumatic brain injuries have recently been put under the spotlight as one of the most important causes of accidental brain dysfunctions. Significant experimental and modeling efforts are thus ongoing to study the associated biological, mechanical and physical mechanisms. In the field of cell mechanics, progresses are also being made at the experimental and modeling levels to better characterize many of the cell functions such as differentiation, growth, migration and death, among others. The work presented here aims at bridging both efforts by proposing a continuum model of neuronal cell submitted to blast loading. In this approach, cytoplasm, nucleus and membrane (plus cortex) are differentiated in a representative cell geometry, and different material constitutive models are adequately chosen for each one. The material parameters are calibrated against published experimental work of cell nanoindentation at multiple rates. The final cell model is ultimately subjected to blast loading within a complete fluid-structure interaction computational framework. The results are compared to the nanoindentation simulation and the specific effects of the blast wave on the pressure and shear levels at the interfaces are identified. As a conclusion, the presented model successfully captures some of the intrinsic intracellular phenomena occurring during its deformation under blast loading and potentially leading to cell damage. It suggests more particularly the localization of damage at the nucleus membrane similarly to what has already been observed at the overall cell membrane. This degree of damage is additionally predicted to be worsened by a longer blast positive phase duration. As a conclusion, the proposed model ultimately provides a new three dimensional computational tool to evaluate intracellular damage during blast loading.

Keywords

continuum model; neuron; blast; cell damage; traumatic brain injury

1. Introduction

The drastic increase of blast-induced traumatic brain injuries both among military—nearly 50% of the Iraq war injured returnees—and civilian casualties—mainly due to terrorists explosive devices—have generated important research efforts in the last few years [1, 2]. Impact- and/or acceleration-induced brain traumatic injuries have already been the focus of many cellular and macroscopical studies through *in vivo* [3, 4, 5, 6, 7, 8, 9, 10], *ex vivo* [11, 12], *in vitro* [13, 14, 15, 16, 17], medical postanalysis [18, 19, 20] or modeling approaches [21, 22, 23, 24, 25, 26, 27, 28, 29, 30, 31, 32, 33, 34]. However the specific effects of a blast

[1]Corresponding authors: antoine.jerusalem@imdea.org, mingdao@mit.edu.

—a pressure wave of finite amplitude generated by a rapid release of energy [35]—on the brain is still widely unkown.

Blast overpressure, or “primary”, injuries have been known for close to 70 years, and extensively observed since in lungs, eyes, ears, the upper respiratory tract, heart, abdomen and more recently brain [36]. The recent wars in Iraq and Afghanistan have further exarcerbated the awareness of the existence of specific mechanisms of blast injuries in the brain [37, 1, 38]. Many neuropathological and neurological injuries have already been referenced for both animal models and humans [2]. At the cellular level, degradation of the cytoskeleton, changes in neurotransmitters, disruption of calcium homeostasis, mitochondrial disturbances, loss in membrane permeability and even altered gene expression have been observed [38, 17]. More specifically, studies of cellular response after blast events provide evidence of degenerative processes in the neuron itself, not only through necrotic pathways but also through apoptotic pathways—or programmed cell death—at the origin of most brain dysfunctions [39, 38, 2].

Technical improvements now allow for *in vivo* study of direct blast effects on animal brain without significantly invading the brain tissue [40, 41], as well as *ex vivo* study able to quantify the accompanying functional damage [12]. Additionally, a vast array of *in vitro* techniques involving barotrauma chamber, rapid acceleration injury device or shockwave generator also allows for more flexibility but at the cost of not taking into account the real environment provided under *in vivo* settings [42, 43]. A wider set of experiments ranging from simple stretch and isostatic pressurization to weight drop and stylus laceration are also available to account for non-primary blast injuries, i.e., blast injuries arising from direct impact or penetration—secondary—, collision arising from a fall of/on the subject—tertiary—, or exposure to gaz, fire or related—quartenary [43]. Moreover, a recent study has directly compared *in vivo, in situ* and *in vitro* brain responses submitted to different indentation rates [44], thus paving the way for more realistic constitutive models of brain tissue under high rate loadings. Coupled to these experimental testing improvements, new imaging techniques now reach submicrometer resolution [45].

In parallel to these experimental efforts, recent complex large scale parallel computational models accounting for fluid-solid interaction effects—between the air blast and multiple organs in the cranium—now allow for pressure extrema localization, and identification of more complex electromagnetic coupling effects with a very high precision [46, 47, 48].

At the cellular level, many groups have been focusing their efforts on the development of mechanical models of the deformation of individual cells or cell parts [49, 50, 51, 52, 53, 54, 55, 56, 57, 58, 59, 60, 61, 62, 63, 64, 65, 66, 33, 67, 68, 69, 70, 71, 72, 73, 74, 75, 76, 77, 78, 79]. For instance, significant progresses have been made on red blood cell (RBC) modeling, with full three dimensional models using finite-element based continuum methods [53, 64], coarse-grained molecular dynamics (MD) simulations [80, 81], and dissipative particle dynamics (DPD) computations capable of describing detailed cell-fluid interactions [82]. These RBC models have been successfully applied to study diseases such as malaria [83, 82]. Developing computational models for cells with nucleus and three-dimensional cytoskeleton network, however, has been much more challenging than that for RBCs with a much simpler cytoskeleton structure and no nucleus.

Among the different techniques proposed in the literature to describe the mechanics of living cells with nucleus and 3D cytoskeleton, the most noticeable involve: modeling the cytoskeleton as a simple mechanical elastic, viscoelastic or poro-viscoelastic continuum [59, 60], as a porous gel or soft glassy material [68], or as a “tensegrity” network incorporating discrete structural elements that bear compression [69]. At a smaller scale, cytoskeleton

proteins and their interaction with the membrane have been more recently modeled using molecular dynamics (MD), coarse-grained MD and normal mode analysis [84, 85, 86], but the important length and time scale limitations of MD coupled to the large number of unknowns either for the atomic interaction potentials or the protein interaction mechanisms forbid its use at the cellular scale. Overall, it is observed that continuum models are flexible enough to allow for a relatively accurate representation of the cell parts geometry (e.g., nucleus, cytoplasm and membrane/cortex) with individualized constitutive macroscopic features of the deformation [49, 50, 52, 55, 57, 62, 61, 63, 65, 66, 70, 68, 69, 33, 71, 72, 74, 75, 78, 79].

Except for a few exceptions, very little work has been dedicated to using such models under damaging—or at least at high—rate loading conditions [33, 75, 76, 78]. Such studies present the inconvenient of bringing more often than not additional unknowns to the problem but under loading rates fast enough to generally avoid the active deformation of the cell, i.e., the self-reorganization of its protein structures under external stimuli. As a consequence, continuum models *a priori* provide an adequate framework for neuron modeling under blast loading. Finally, to the best of the knowledge of the authors, direct simulations of the damaging effects of the blast of a cell with components differentiation has still not been achieved (note that Miller *et al*. presented a model of a cell subjected to stress waves but focused on cell-substrate decohesion [87, 75]).

In this work, we thus propose a continuum model with differentiated nucleus, cytoplasm and membrane/cortex. Each one of these components is described by a visco-hyperelastic constitutive model. These models are purposefully chosen as simple as possible to describe adequately the different deformation mechanisms while reducing the size of the model parameters space. The model is calibrated against published nanoindentation experimental results at multiple rates [76] and a fluid-structure interaction continuum model of the calibrated cell is submitted to a blast wave. Section 2 introduces the constitutive framework and the finite element setup for the simulations. The calibration of the model against nanoindentation experimental work is presented in Section 3 and the final blast simulation is shown in Section 4. Finally, the results are discussed and related to experimental studies in Section 5.

2. Numerical setup

In this section, the visco-hyperelastic constitutive framework of all three modeled components is presented followed by a description of the finite element model discretization and parametrization.

2.1. Constitutive framework

2.1.1. General equations—The three main modeled cell components (cortex-membrane, cytoplasm and nucleus) are assumed to follow a visco-hyperelastic mechanical behavior.

For isotropic hyperelastic materials, it is generally assumed that a Helmholtz free energy function Ψ can be defined as a function of the Jacobian J and the modified strain invariants $\bar{I}_1$ and $\bar{I}_2$ [88].

The stress measure conjugated to the right Cauchy-Green tensor **C**, the second Piola Kirchhoff stress **S**, is then given by

$$\mathbf{S}=2\frac{\partial\Psi}{\partial\mathbf{C}} \quad (1)$$

2.1.2. Generalized Maxwell model—The viscoelastic formulation used here is based on the work of Taylor, Pister and Goudreau (1970) [89].

The generalized Maxwell model is a rheological model composed of a Hooke model (i.e., a spring) and a given number of Maxwell models—a Hooke model and a Newton model (i.e., a dashpot) in series—in parallel [90]. In order to minimize the number of model parameters, we couple the hyperelastic model defined earlier with a generalized Maxwell model composed of only one Maxwell component, see Figure 1. It is the simplest model allowing for the consideration of both long term and short term elasticity with a viscous effect.

In Figure 1, μ_0, μ_1 and η_1 are respectively the long term shear modulus, and the shear modulus and viscosity associated to the Maxwell component. $\mathbf{\Gamma}$ is the internal variable, a strain measure, associated to the dashpot. The tensor $\mathbf{S}_{\text{vis}}$ characterizes the viscous relaxation due to a viscous Newtonian fluid and is representative here of all viscous effects arising in each one of the three components of the cell. It should be noted that these effects are restricted to the isochoric deformation mode. The reader is also invited to refer to Ref. [88] for more details on theory and implementation.

2.1.3. Neo-Hookean model—As already stated previously, the work presented here aims at minimizing the number of parameters. As a consequence, the neo-Hookean model is chosen for all cell components. This model only depends on the Jacobian and the first strain invariant. The associated long term volumetric and isochoric strain energy functions are given by [88]

$$\left\{ \begin{array}{lcl} \Psi^{\infty}_{vol}(J) & = & \frac{1}{d_0}(J-1)^2 \\ \Psi^{\infty}_{iso}(\bar{I}_1) & = & c_0(\bar{I}_1 - 3) \end{array} \right. \tag{2}$$

where $c_0 = \mu_0/2$ (see Section 2.1.2), and d_0 is a material parameter related to the compressibility of the material.

2.1.4. Hugoniot/Mie-Grüneisen equation of state—As long as relatively low strain-rates and pressures are considered, the above description is reliable. However, when very fast material responses under high pressures are considered, such as the ones provoked by a shock wave, the volumetric part of the stress tensor, i.e., the pressure P, must be described by an equation of state. As a consequence, even though such approach is not necessary for the indentation simulation, it is required for the blast simulation.

The shock response of many materials is well described by the Hugoniot relation between the shock velocity U_s and the material velocity U_p of the simple form [91]:

$$U_s = C_0 + sU_p \tag{3}$$

In this expression, C_0 and s are material parameters which can be obtained from experiments.

By considering conservation of mass and momentum in a control volume at the shock front and Equation (3), the final pressure[2] can be calculated explicitly as a function of the Jacobian behind the shock front J_H and the reference density ahead of the shock ρ_0 [92]:

[2]In this section only, the pressure is by convention positive in compression

$$P_H = \frac{\rho_0 C_0^2 (1 - J_H)}{[1 - s(1 - J_H)]^2} \tag{4}$$

where J_H is related to the density ρ_H, the specific volume V_H or the deformation gradients tensor $\mathbf{F}_H$, defined behind the shock front, by:

$$J_H = \frac{\rho_0}{\rho H} = \frac{V_H}{V_0} = det(\mathbf{F}_H) \tag{5}$$

Alternatively, one can use the Mie-Grüneisen Equation of State to relate the pressure P and the internal energy per unit mass E to their respective value on the Hugoniot curve P_H and E_H [91], which leads to

$$P = P_H \left(1 - \frac{\Gamma_0}{2}\left(1 - \frac{\rho_0}{\rho}\right)\right) + \Gamma_0 \rho_0 E \tag{6}$$

where Γ_0 is the Grüneisen parameter at the initial state.

Finally, the internal energy rate per unit mass is given by the first law of thermodynamics as the sum of the volumetric and deviatoric work rate and heat rate $\dot{Q}$ [91]:

$$\dot{E} = -\frac{1}{\rho}\left(\frac{P\dot{\rho}}{\rho} + \dot{\Psi}_{iso}\right) + \dot{Q} \tag{7}$$

where use has been made of the deviatoric strain energy function, and where C_V is the specific heat capacity at constant volume and T the temperature.

Additionally, the shock response can be considered as an adiabatic process: $\dot{Q} = 0 J.kg^{-1}.s^{-1}$. Note that the pressure release is actually isentropic, in general relatively close to the adiabatic process; as a consequence, the whole event can be assumed as adiabatic [91].

The temperature can then be extracted easily from:

$$\dot{E} = C_v \dot{T} \tag{8}$$

An artificial viscosity scheme (necessary for shock wave propagation) is finally used (a complete description is provided in Supplementary Materials A-3).

2.2. Finite element model

The main components that regulate the mechanical properties of the cell are the membrane, the cytoplasm (composed of cytoskeleton and organelles bathing in a rheological fluid: the cytosol) and the nucleus [60]. The cytoskeleton is a dynamic structure that maintains the cell shape, protects it, enables cellular motion and plays important roles in all cellular processes. It contains three main mechanical structures with different functionalities: actin filaments, intermediate filaments, and microtubules. The cell membrane is a semipermeable lipid bilayer that separates the interior of a cell from the outside. The cytoskeleton is found underlying the cell membrane in the cytoplasm and provides a scaffolding for membrane proteins to anchor to, as well as for forming organelles that extend in and out of the cell. In fact, cytoskeletal elements interact extensively and intimately with the cell membrane creating a region, situated just under the membrane, densely populated with proteins: the

cortex [93]. Finally, the cell nucleus contains most of the cell's genetic material and is therefore the control center of the cell.

In the following, we detail the finite element discretization setup for the calibration (nanoindentation) simulations and for the blast simulation. The finite element software Abaqus was used for the simulations [94].

2.2.1. Nanoindentation finite element setup—We propose here to follow the same overall geometry of a semi-spheroid as in Ref. [76] but focusing more on the intrinsic structures of the neuron, while simplifying the constitutive models for each modeled part, rather than adopting a more complex representative constitutive law for the full neuron cell. The chosen modeled continua are the nucleus, the cytoplasm and the cortex plus membrane.

The model size is based upon the average height and diameter experimentally observed (out of 79 observations) by Bernick *et al.*: height of 7.9 μm for a diameter of 16.8 μm [76]. The nucleus is then considered as having a volume of one third of the total cell volume [65]. Its dimensions are chosen such that the ratio of the diameters and heights of the full neuron cell and the nucleus be the same, i.e., diameter and height are respectively 11.65 μm and 5.48 μm. The nucleus is centered in the middle of the cell. The thickness of the "membrane plus cortex" region is estimated to be in the range of 100 nm—400 nm [57, 60]. As a compromise, the value of 200 nm is chosen here. For the indentation simulation, the axisymmetry of the problem allows for the use of a 2D axisymmetric mesh. The final mesh is shown in Figure 2. More details on the regions of interest, geometry and finite element mesh are given in Supplementary Materials A-1.

Boundary and loading conditions are following the setup found in Ref. [76]. The bottom part is fixed in all directions, consistent with the experimental observation that the neuron is in slipless contact with its substrate [76]. Usual axisymmetric boundary conditions are specified along the axis of revolution. Finally, a 45 μm diameter spherical bead is used for the nanoindentation and is modeled as an analytical rigid surface. The loading pattern is the following: a first indentation at 0.3 $\mu m.s^{-1}$ until a force of roughly 0.3 nN is measured; a plateau at the same position for 15 s; three load-unload cycles to 2 μm additional depth at three increasing rates 10 $\mu m.s^{-1}$, 1 $\mu m.s^{-1}$ and 0.1 $\mu m.s^{-1}$ respectively; a final load at 10 $\mu m.s^{-1}$ and a plateau at this depth for 120 s. See Ref. [76] for more details. Table 1 gathers the different loading steps as used in this reference.

A static implicit scheme is used for the nanoindentation simulation. Spatial convergence was verified. Note that the rates are small enough to neglect inertial effect (the Reynolds numbers for the different model parts are in the range of $2 \times 10^{-17} - 10^{-7}$), and thus there is no need for dynamic simulations in this case.

2.2.2. Blast finite element model setup—For the blast simulation, the previous cell model geometry is extended to 3D with the same height and diameter and embedded at the bottom of a 100 μm×100 μm×100 μm cubic fluid box. The final model is shown in Figure 3. More details are given in Supplementary Materials A-2.

The overpressure loading of a shock wave as emitted by a shock tube is typically of the order of hundreds of kPa (i.e., a few atm) with duration of the order of 1 ms [95]. However, recent *in vitro* studies of blast loading of cells have been using laser-induced shock wave to study cell injury under blast [96], as well as cell adhesion [87, 75]. For such waves, the overpressure is of the order of 50 MPa [96] and the duration of the order of 5 ns for a Gaussian laser pulse [87].

Because the work proposed here is oriented towards the comparison of simulations with *in vitro* experiments, the pressure pulse used on the top face of the model is following the latter description: a constant applied pressure of 50 *MPa* for 5 *ns*.

3. Nanoindentation simulation

An extensive survey of the model parameter values as they can be found in the literature is provided in Supplementary Materials B.

For the three cell components, incompressibility is considered as is commonly done for biological cells [50, 51, 54, 53, 57, 59, 61, 71, 73, 77, 74, 76, 75]. Based on the incompressibility of the three regions, the Poisson's ratio is taken to be $\nu = 0.5$ ($d_o = 0$) for all regions. It should be emphasized though that other studies have suggested compressibility [97, 72, 79], in some cases with significant effects on the deformation mechanisms [72]. However, in view of the lack of consensus and the fact that, under shock loading (see Section 4), there is *a priori* not enough time for viscosity and/or volume change to occur, this value of 0.5 is chosen as a first approximation.

In view of the literature review, the value of 1000 *Pa* is chosen for the membrane/cortex Young's modulus (c_0^{mem}=166.67 *Pa*) and the relaxation time τ_1^{mem} is taken as 3000 *s* (see Supplementary Materials B-1). In the following, we determine the remaining parameters by calibrating them against the averaged experimental nanoindentation curve of Ref. [76], and validate them by comparing simulation and experiment for another cell-specific nanoindentation test [76].

It should finally be emphasized that in the proposed model, the adhesion between cell and bead is not taking into account as a first approximation; the reader is referred to Ref. [70] for a modeling approach accounting for it.

3.1. Initial indentation depth and Young's moduli calibration

As described in Section 2.2.1, the initial loading rate (0.3 $\mu m.s^{-1}$) is maintained until F_B = 0.3 *nN* is reached (Stages A and B in Table 1). Depending on the cell height, the indentation depth at which such load is reached consequently varies. Additionally, the final plateau of the loading at Stage E, is yielding approximatively a force of F_E = 1.67 *nN* in the average experimental curve [76].

Note that Hertz' contact law does not apply here because of the multiple material stiffnesses of the cell regions. Both plateaux of Stages B and E reach a steady-state value, viscous-independent by definition. As such, the only two remaining parameters of influence are the Young moduli of the cytoplasm and the nuclei, E_0^{cyto} and E_0^{nuc}. Assuming a factor of 4 difference between the two values (see Supplementary Materials B-2), the set of unknown values defining both plateaux is narrowed down to two parameters only: δ_0 and E_0^{nuc} (or E_0^{cyto}). Additionally, assuming that the contact is made in a similar way as Hertz' law but leaving the exponent n (fixed at 3/2 in Hertz' law) as a free parameter, one reaches:

$$\frac{\delta_0+2}{\delta_0}=\left(\frac{F_E}{F_B}\right)^n \tag{9}$$

This relation mathematically guarantees that the pair of unknowns (δ_0, E_0^{nuc}) is uniquely defined by the pair (F_B, F_E). After calibration, we finally reach:

$$\begin{cases} \delta_0 = 1.41 \mu m \\ c_0^{nuc} = E_0^{nuc}/6 = 6.67\ Pa \\ c_0^{cyto} = E_0^{cyto}/6 = 1.66\ Pa \end{cases} \quad (10)$$

Note that the nucleus and cytoplasm values are in the lower range of the literature values (see Supplementary Materials B-2).

3.2. Viscosity parameters calibration

Because all cell parts are taken as incompressible, viscosity parameters are only defined for the shear component. The main difficulty of this calibration resides in the fact that a set of five parameters need to be defined: the relaxation times τ_1^{nuc} and τ_1^{cyto}, the viscosities η_1^{nuc} and η_1^{cyto} for nucleus and cytoplasm, but also η_1^{mem} for the membrane/cortex. By considering that the factor of 4 between the long term shear moduli of cytoplasm and nucleus is also valid for the shear moduli associated to the Maxwell components μ_1 (see Figure 1), the space of parameters is reduced to four unknowns: τ_1^{nuc}, τ_1^{cyto}, η_1^{nuc} (or η_1^{cyto}) and η_1^{mem}. Note that picking a pair (τ_1, η_1) is equivalent to picking (τ_1, μ_1); in the following we use the latter.

Despite the fact that simple viscous models have been chosen, the number of unkowns is relatively high. However, the advantage of having three cycles and two relaxation periods to fit the model is that each parameter is observed to influence the simulated curve in different ways. Without being able to fully guarantee the uniqueness of the parameters, we empirically observed that, around the final chosen values: a change in τ_1^{nuc}, and τ_1^{cyto} affect the relaxation of the fast and slow cycles respectively, μ_1^{nuc} (or μ_1^{cyto}) affect the peak values of the reaction forces at the maximum indentations, and μ_1^{mem} affects more lightly most of the curve. As a consequence, most of the parameters have been calibrated by considering independently their action on the reaction-indentation curve patterns, μ_1^{mem} being use to finalize the final fit. The final set of parameters is given in Table 2 and the set of curves for the simulated three cycles (done successively within the same simulation, as done experimentally) and the experimental curves taken from Ref. [76] are shown in Figures 4, 5 and 6. A good fit is obtained and the simulation results are well within the experimental error bars (not shown here, see Ref. [76]).

Note that the viscoelastic time constants for the nucleus and the cytoplasm $\tau_1^{nuc/cyto}$ are in good agreement with literature values (see Supplementary Materials B-2). Similarly, the membrane viscosity (η_1^{mem}=41.67 *kPa.s*) agrees by a bit less than one order of magnitude with literature values (see 375 *kPa.s* in Supplementary Materials B-1) and the nuclear viscosity (η_1^{nuc}=431.11 *Pa.s*) also lies within the literature range (see 52—1200 *Pa.s* in Supplementary Materials B-2).

However, cytoplasmic viscosity (η_1^{cyto}=1.08 *Pa.s*) is found to be smaller by one to two orders of magnitude with full cytoplasm values (see 26—600 *Pa.s* in Supplementary Materials B-2) but is just in the lower range of crosslinked/bundled actin network (see ~1—500 *Pa.s* in Supplementary Materials B-2).

It must be finally emphasized that literature values are gathered for a wide range of cell types and sometimes with a wide range of values for a same given cell. The observed discrepancy can be due to different experimental procedures, approximated modeling choices and/or differences in the culture of the cells. As a consequence, we complement this

calibration by an additional validation step and compare simulation and experiment for one additional cell-specific nanoindentation test [76].

3. 3. Validation

The validation is done by comparing the experimental results for another specific representative cell (as opposed to the average response from the previous section) with a diameter of 14.2 μm and height of 7.6 μm, similarly to what is done in Ref. [76], from which the experimental results are extracted.

The mesh presented in Section 2.2.1 was modified to account for the change of height and diameter and all the parameters, except δ_0, were taken from Table 2. δ_0 was then adjusted to reach the inital force of 0.3 nN for the cell and the same loading pattern as before was used for the simulation. A value 0.84 nm for δ_0 was found. The final indentation force at each of the three maxima in each of the three cycles was extracted and compared to the experimental results, see Table 3.

Taking into account the large variability of the cell geometry (experimental error, non-constant diameter and nucleus position within the cytoplasm, among others), the model always captures the maximum forces within 17% of the experimental value, with an overall average error of 8.4%. These results confirm the ability of the model to capture the main rate-dependent deformation features operative here.

4. Blast simulation

In the following, we use the previously calibrated model and modify the volumetric contribution of the constitutive material model following Section 2.1.4. The new material parameters are then given and the simulation is analyzed. The corresponding stress patterns are finally compared with the ones for the indentation.

4.1. Modifications and new material parameters

4.1.1. Surrounding fluid—The constitutive description of the fluid deformation in the Eulerian mesh being out of the scope of this work, we reduce this section to the parameters decriptions of the surrounding fluid. The reader is invited to refer to the documentation of Abaqus [94] for more information on its implementation.

The Hugoniot/Mie-Grüneisen equation of state presented in Section 2.1.4 has been used successfully for the description of a shock wave propagation in water below 1 GPa, which is the case here [98]. Because water is the main constituent of the surrounding fluids in *in vitro* laser-shock experiments [96], the surrounding fluid in the cubic box is chosen as water, i.e., [98]

$$\begin{cases} \rho_0 = 1000 kg.m^{-3} \\ C_0 = 1450 m.s^{-1} \\ s = 1.99 \end{cases} \tag{11}$$

Additionally, for water at ambient conditions, the Grüneisen parameter, the specific heat capacity at constant volume and the dynamic (newtonian) viscosity η are taken as [99, 100, 101]:

$$\begin{cases} \Gamma_0 \approx 0.1 \\ C_\upsilon = 4184 J.kg^{-1}.K^{-1} \\ \eta \approx 0.001 Pa.s \end{cases} \quad (12)$$

4.1.2. Neuron—As described previously, under shock loading conditions, the volumetric contribution of the stress needs to be described by an equation of state. The Hugoniot/Mie-Grüneisen has been shown to be a good candidate for the description of biomaterials submitted to shock loading [102]. Assuming the compressibility of the cell similar to the one of water (see Section 3), we thus use the water values for ρ_0, C_0, s, Γ_0 and C_V for the cytoplasm and nucleus. Note that because of its shell formulation, the cortex/membrane volumetric constitutive model could not be easily replaced by an equation of state and was kept as hyperelastic as a first approximation.

It must finally be emphasized that the deviatoric contribution of the stress is not assumed to follow the dynamic newtonian viscosity of water, but remains the same as in the indentation model.

4.2. Simulation results

The blast simulation was run until 150 *ns* and the convergence was checked.

Figures 7 and 8 show the pressure and von Mises stress fields for the different regions at 26.88 *s* for the nanoindentation simulation (which corresponds to the first indentation peak, with maximum pressure and von Mises stress) and 65.5 *ns* for the blast simulation (which corresponds to the time at which the wave has crossed half the cell, as a good compromise between the moment the wave hits the membrane and the moment it bounces back from the substrate, thus roughly doubling the pressure level). Note that maximum compression is reached at 70 *ns* in the blast simulation, i.e., the results shown are almost the ones at maximum deformation. Figure 9 shows the temperature increase for the whole cell during the blast event. The videos of the pressure field evolution during the blast for the whole mesh, as well as for the individual cell parts are available as Supplementary Materials.

Figure 7 shows that whereas the pressure is mainly concentrated in the cytoplasm and top of nucleus right underneath the indentor in the nanoindentation case, it is following the wave along the horizontal propagating plane in the blast case. Furthermore, the pressure is discontinuous in the former case along the interfaces cortex-cytoplasm (with a jump of ~ 300 *Pa*) and cytoplasm-nucleus (with a jump of ~ 30 *Pa*), and continuous in the latter. It can thus be concluded that the blast event propagates hydrostatic stress in a less material-discriminatory way than it is done at slower rate deformations.

Interestingly, the von Mises stress levels are of the same orders of magnitude for both simulations (see Figure 8) with maxima of ~ 10—100 *Pa*. Note that this result is even more surprising considering the fact that the typical cell viscosity charateristic time is of the same order of magnitude as our nanoindentation duration (*s*) [66], but much larger than the one of the blast event (*ns*). However, if shearing forces are mainly concentrated within the nucleus for the nanoindentation case, the maxima can be identified at the interfaces for the blast case.

Finally, it can be seen from Figure 9 that the temperature is rising by ~ 0.1 °*C*.

5. Discussion

The high pressure (~ 50 *MPa*) is propagated directly from water into the cell, and in between cell parts, mainly because of the lack of volumetric impedance mismatch (equation of state parameters are the same). It could be thus relevant to have accurately calibrated parameters for each part of the cell in order to observe the effect of such possible mismatches. However, the volumetric material parameters would still remain relatively similar, and a drastic change in pressure should not be expected. Based on brain tissue studies [47], such high pressure should *a priori* be sufficient to cause a high degree of brain damage. This conclusion is confirmed by the fact that the rates used here are much higher than the ones used as tissue damage criteria in other works on impact [25, 26] or blast [47, 95].

Other works have focused directly on the cell by increasing the pressure up to ~ 2 *M Pa* (20 *atm*) over a period of 6 *s*, sustaining it from 1 to 10 *min* [42]. If such work leaves aside the rate effects, it has the benefit to identify independently the effect of sustained pressure on cell components. More precisely, membrane damage was observed above 10 *atm*, eventually leading to irreversible damage under sufficient pressure and duration [42]. Additonal works have similarly focused on the effect of such high hydrostatic pressure on cell functions such as migration [103]. By studying the release of fatty acids and lactate dehydrogenase into the extracellular medium under different pressure levels/durations, Murphy and Horrocks [42] identified damage thresholds for different types of cells. They proposed that under high pressure, the membrane acyl chains motion is reduced as they condense to accomodate their volume decrease. Doing so, the viscosity is reduced and the “fluid behavior” of the membrane is modified to a stiffer configuration, eventually leading to receptor damages [42]. Along the same lines, recent work by Alford *et al.* suggests that under rapid blast driven stretch, cellular membrane integrins stimulation is altered, thus potentially modifying calcium dynamics and phenotypic behavior in the concerned cells [17].

Such experimental findings are corroborated by the von Mises stress fields in Figure 8. These results show that one of the main features of a blast event is the localized concentration of the von Mises stress at the interfaces within the blast wave plane. The resulting interface shearing effect could have drastic implications on the organization of receptors, transmembranes organelles, and associated cytoskeletal components (for instance, in the cortex). The coupling effect of membrane receptor mechanical loading due to pressure and interface shearing could thus lead to their alterations. More specifically, the loss of membrane integrity, despite the presence of reversible repair mechanisms below some pressure/duration limits, is a common damaged area in all catastrophic types of cell death. For instance, apoptosis and F-actin cortex detachement from the membrane have been directly related [104], and direct relation between cell death and loss of membrane integrity has also been observed in necrosis and necroptosis [105, 106, 107]. The recent work of Alford *et al.* on the integrin alteration role in phenotypic switching confirms that point [17]. Note finally that, to the best of the knowledge of the authors, experimental findings of loss of integrity of the nucleus membrane have not been reported. However, the model predicts similar shearing stress levels at both the nucleus membrane and the overall cell membrane, and thus potential similar damage patterns for both the nucleus and cell membranes.

Using shock tube experimental setups with different configurations, Reneer *et al.* have recently highlighted a direct correlation between a longer positive phase duration and a higher level of damage at equal peak pressure [41]. In order to compare this experimentally observed trend to our numerical predictions, the initial shock positive phase duration was extended from 5 *ns* to 10 *ns* and 15 *ns*. The pressure, von Mises, longitudinal (in the shock direction) strain and longitudinal strain-rate evolutions for a material point situated along the interface between cytoplasm and nucleus and at roughly 75 % of the total height of the

nucleus were extracted, see Figure 10. The results confirm the experimental findings by predicting higher pressure, von Mises stress, strain and strain-rate with increasing durations. The von Mises stress level, more particularly, has been found to increase proportionally with the duration (doubling and tripling for doubled and tripled durations), thus potentially agravating the effect of shearing at the interface. The strain-rate, however, was found to increase moderately.

As a consequence, our simulations confirm that laser induced shock wave experiments on cell lead to interface damage within the cell. The fact that a blast wave seems to concentrate shear forces at these particular regions, while potentially debilitating some of its functions through pressure-dependent membrane structural reorganization is even more relevant for neurons. Indeed, whereas large strains seem to be sustained by axon membrane at low rates, high rates deformation are known to drastically affect the conduction and thus functional properties of the axons [108]. This confirms that the model prediction of shear localization at the cortex, potentially exacerbated by a longer positive phase duration, has direct implications on the functional properties of the neuron, and thus the brain.

Finally, the temperature rise (see Figure 9) can *a priori* be judged as too small to damage the cell and/or affect the cell's health. Accordingly, if thermal shock has been shown to have a significant impact on cytoskeletal organization, potentially leading to microtubule malfunctions [109], the experimental temperature change used in this reference are two orders of magnitude higher than here. However, it must be emphasized that the increase of $0.1\ ^\circ C$ observable in the cell is achieved in roughly 5 *ns*, which corresponds to a rate of 20 million $^\circ C.s^{-1}$. It is thus not clear if the temperature rate itself, and not just the level reached can be relevant to the cell health. Molecular dynamics studies could potentially allow for further investigations in this direction.

6. Conclusion

In this work, a comprehensive continuum model of a neuron was presented. This model involves the consideration of three independent regions: the nucleus, the cytoplasm and the cortex plus membrane. Each region is decribed by a constitutive model based on visco-hyperelasticity and equation of state, for high rate/pressure loadings. The parameters that were not taken out of the literature were calibrated against published experimental multi-rate indentation results. Finally, a blast event within typical *in vitro* conditions was simulated.

The results show that, whereas pressure level is affecting the cell homogeneously, shearing effects are, on the contrary, mainly observed at the interfaces. This phenomenon has been shown to be critically important for the cell membrane integrity and health, confirming what was observed at the cell function level experimentally. Finally, both the pressure and von Mises stress, and thus the potential damage, have been observed to increase significantly with increased positive phase duration of the shock wave.

As a conclusion, the presented model successfully captures some of the intrinsic intracellular phenomena occurring during the neuron rate-dependent deformation and potentially leading to damage. It also predicts that the nucleus membrane is likely to suffer from the same type of damage as the one observed for the cell membrane. Ultimately, the proposed model constitutes a novel numerical tool able to predict some of the most complex cell deformation mechanisms occurring during TBI.

Supplementary Material

Refer to Web version on PubMed Central for supplementary material.

Acknowledgments

The authors would like to thank Prof. Subra Suresh for his insightful guidance and suggestions. The authors are also grateful to Javier Rodriguez from Principia for its unmeasurable help with Abaqus. A.J. acknowledges support from the Juan de la Cierva grant from the Spanish Ministry of Science and Innovation, from the Amarout grant from the European Union, from the ESTRUMAT-S2009/MAT-1585 grant (Madrid Regional Government), and from the Cajal Blue Brain Project. M.D. acknowledges support from the National Institutes of Health (NIH) Grant R01HL094270, Infectious Disease Interdisciplinary Research Group of the SMART Center, and the Computational Systems Biology Programme of the Singapore–MIT Alliance (SMA).

References

1. Moore DF, Jaffee MS. Military traumatic brain injury and blast. NeuroRehabilitation. 2010; 26(3): 179–181.10.3233/NRE-2010-0553 [PubMed: 20448307]
2. Hicks RR, Fertig SJ, Desrocher RE, Koroshetz WJ, Pancrazio JJ. Neurological effects of blast injury. The Journal of TRAUMA Injury, Infection, and Critical Care. 2010; 68(5):1257–1263.10.1097/TA.0b013e3181d8956d
3. Khan M, Im Y-B, Shunmugavel A, Gilg AG, Dhindsa RK, Singh AK, Singh I. Administration of S-nitrosoglutathione after traumatic brain injury protects the neurovascular unit and reduces secondary injury in a rat model of controlled cortical impact. Journal of Neuroinflammation. 2009; 6(32):1–12.10.1186/1742-2094-6-32 [PubMed: 19123954]
4. Norris CM, Scheff SW. Recovery of afferent function and synaptic strength in hippocampal CA1 following traumatic brain injury. Journal of Neurotrauma. 2009; 26(12):2269–2278.10.1089/neu.2009.1029 [PubMed: 19604098]
5. Hunt RF, Scheff SW, Smith BN. Posttraumatic epilepsy after controlled cortical impact injury in mice. Experimental Neurology. 2009; 215:243–252.10.1016/j.expneurol.2008.10.005 [PubMed: 19013458]
6. Shafieian M, Darvish KK, Stone JR. Changes to the viscoelastic properties of brain tissue after traumatic axonal injury. Journal of Biomechanics. 2009; 42(13):2136–2142.10.1016/j.jbiomech.2009.05.041 [PubMed: 19698945]
7. Kharatishvili I, Sierra A, Immonenb RJ, Gröhn OHJ, Pitkänen A. Quantitative T2 mapping as a potential marker for the initial assessment of the severity of damage after traumatic brain injury in rat. Experimental Neurology. 2009; 217(1):154–164.10.1016/j.expneurol.2009.01.026 [PubMed: 19416663]
8. Chena G, Zhang S, Shi J, Ai J, Qi M, Hang C. Simvastatin reduces secondary brain injury caused by cortical contusion in rats: Possible involvement of TLR4/NF-κB pathway. Experimental Neurology. 2009; 216(2):398–406.10.1016/j.expneurol.2008.12.019 [PubMed: 19166837]
9. Schwetye KE, Cirrito JR, Esparza TJ, Mac Donald CL, Holtzman DM, Brody DL. Traumatic brain injury reduces soluble extracellular amyloid-β in mice: A methodologically novel combined microdialysis-controlled cortical impact study. Neurobiology of Disease. 2010; 40(3):555–564.10.1016/j.nbd.2010.06.018 [PubMed: 20682338]
10. Kabadi SV, Hilton GD, Stoica BA, Zapple DN, Faden AI. Fluid-percussion-induced traumatic brain injury model in rats. Nature Protocols. 2010; 5(9):1552–1563.10.1038/nprot.2010.112
11. Ouyang H, Galle B, Li J, Nauman E, Shi R. Biomechanics of spinal cord injury: A multimodal investigation using ex vivo guinea pig spinal cord white matter. Journal of Neurotrauma. 2008; 25:19–29.10.1089/neu.2007.0340 [PubMed: 18355155]
12. Connell S, Gao J, Chen J, Shi R. Novel model to investigate blast injury in the central nervous system. Journal of Neurotrauma. 2011; 28:1229–1236.10.1089/neu.2011.1832 [PubMed: 21529318]
13. Geddes DM, Cargill RS, LaPlaca MC. Mechanical stretch to neurons results in a strain rate and magnitude-dependent increase in plasma membrane permeability. Journal of Neurotrauma. 2003; 20(10):1039–1049.10.1089/089771503770195885 [PubMed: 14588120]
14. Geddes-Klein KSDM, Meaney D. Mechanisms and consequences of neuronal stretch injury in vitro differ with the model of trauma. Journal of Neurotrauma. 2006; 23(2):193–204.10.1089/neu.2006.23.193 [PubMed: 16503803]

15. LaPlaca MC, Prado GR. Neural mechanobiology and neuronal vulnerability to traumatic loading. Journal of Biomechanics. 2010; 43(1):71–78.10.1016/j.jbiomech.2009.09.011 [PubMed: 19811784]
16. Ziegler L, Segal-Ruder Y, Coppola G, Reis A, Geschwind D, Fainzilber M, Goldstein RS. A human neuron injury model for molecular studies of axonal regeneration. Experimental Neurology. 2010; 223(1):119–127.10.1016/j.expneurol.2009.09.019 [PubMed: 19804775]
17. Alford PW, Dabiri BE, Goss JA, Hemphill MA, Brigham MD, Parker KK. Blast-induced phenotypic switching in cerebral vasospasm. PNAS. 2011; 108(31):12705–12710.10.1073/pnas.1105860108 [PubMed: 21765001]
18. Barnes PD, Krasnokutsky MV, Monson KL, Ophoven J. Traumatic spinal cord injury: accidental versus nonaccidental injury. Seminars in Pediatric Neurology. 2008; 15(4):178–184.10.1016/j.spen.2008.10.009 [PubMed: 19073323]
19. Hoffman SW, Harrison C. The interaction between psychological health and traumatic brain injury: a neuroscience perspective. The Clinical Neuropsychologist. 2009; 23:1400–1415.10.1080/13854040903369433 [PubMed: 19882478]
20. Yoganandan N, Baisden JL, Maiman DJ, Gennarelli TA, Guan Y, Pintar FA, Laud P, Ridella SA. Severe-to-fatal head injuries in motor vehicle impacts. Accident Analysis and Prevention. 2010; 42(4):1370–1378.10.1016/j.aap.2010.02.017 [PubMed: 20441854]
21. Willinger R, Baumgartner D, Guimberteau T. Dynamic characterization of motorcycle helmets: modelling and coupling with the human head. Journal of Sound and Vibration. 2000; 235(4):611–625.10.1006/jsvi.1999.2931
22. Gilchrist MD, O'Donoghue D, Horgan T. A two-dimensional analysis of the biomechanics of frontal and occipital head impact injuries. International Journal of Crashworthiness. 2000; 6(2):253–262.10.1533/cras.2001.0176
23. Willinger R, Baumgartner D, Chinn B, Schuller E. New dummy head prototype : development, validation and injury criteria. International Journal of Crashworthiness. 2000; 6(3):281–294.10.1533/cras.2001.0178
24. Guillaume AI, Osmont D, Gaffié D, Sarron J-C, Quandieu P. Physiological implications of mechanical effects of +Gz accelerations on brain structures. Aviation, Space, and Environmental Medicine. 2002; 73(3):171–177.
25. Willinger R, Baumgartner D. Human head tolerance limits to specific injury mechanisms. International Journal of Crashworthiness. 2003; 8(6):605–617.10.1533/ijcr.2003.0264
26. Willinger R, Baumgartner D. Numerical and physical modelling of the human head under impact – towards new injury criteria. International Journal of Vehicle Design. 2003; 32(1 - 2):94–115.10.1504/IJVD.2003.003239
27. Horgan TJ, Gilchrist MD. The creation of three-dimensional finite element models for simulating head impact biomechanics. International Journal of Crashworthiness. 2003; 8(4):353–366.10.1533/ijcr.2003.0243
28. Zhang L, Yang KH, King AI. A proposed injury threshold for mild traumatic brain injury. Transactions of the ASME. 2004; 126:226–236.
29. Horgan TJ, Gilchrist MD. Influence of FE model variability in predicting brain motion and intracranial pressure changes in head impact simulations. International Journal of Crashworthiness. 2004; 9(4):401–418.10.1533/ijcr.2004.0299
30. Raul J-S, Baumgartner D, Willinger R, Ludes B. Finite element modelling of human head injuries caused by a fall. International Journal of Legal Medicine. 2006; 120(4):212–218.10.1007/s00414-005-0018-1 [PubMed: 16059711]
31. El Sayed T, Mota A, Fraternali F, Ortiz M. Biomechanics of traumatic brain injury. Computer Methods in Applied Mechanics and Engineering. 2008; 197(51 - 52):4692–4701.10.1016/j.cma.2008.06.006
32. Deck C, Willinger R. Improved head injury criteria based on head FE model. International Journal of Crashworthiness. 13(6):667–679.10.1080/13588260802411523
33. Abolfathi N, Karami G, Ziejewski M. Biomechanical cell modeling under impact loading. International Journal of Modelling and Simulation. 2008; 28(4):470–476.10.2316/Journal.205.2008.4.205-4877

34. Motherway J, Doorly MC, Curtis M, Gilchrist MD. Head impact biomechanics simulations: a forensic tool for reconstructing head injury? Legal Medicine. 2009; 11(1):S220–S222.10.1016/j.legalmed.2009.01.072 [PubMed: 19261508]
35. Christou G, Young LR, Goel R, Vechart A, Jérusalem A. Soda-lime glass based material attenuates shock in a helmet liner: a fluid-solid interaction continuum model simulation. Int J Impact Eng. 2010; 47:48–59. http://dx.doi.org/10.1016/j.ijimpeng.2012.03.003.
36. Mayorga MA. The pathology of primary blast overpressure injury. Toxicology. 1997; 121:17–28.10.1016/S0300-483X(97)03652-4 [PubMed: 9217312]
37. Warden DL, French LM, Shupenko L, Fargus J, Riedy G, Erickson ME, Jaffee MS, Moore DF. Case report of a soldier with primary blast brain injury. Neuroimage. 2009; 47(2):T152–T153.10.1016/j.neuroimage.2009.01.060 [PubMed: 19457364]
38. Cernak I, Noble-Haeusslein LJ. Traumatic brain injury: an overview of pathobiology with emphasis on military populations. Journal of Cerebral Blood Flow and Metabolism. 2010; 30:255–266.10.1038/jcbfm.2009.203 [PubMed: 19809467]
39. Leung LY, VandeVord PJ, Dal Cengio AL, Bir C, Yang KH, King AI. Blast related neurotrauma: a review of cellular injury. Molecular and Cellular Biomechanics. 2008; 5(3):155–168. [PubMed: 18751525]
40. Chavko M, Koller WA, Prusaczyk WK, McCarron RM. Measurement of blast wave by a miniature fiber optic pressure transducer in the rat brain. Journal of Neuroscience Methods. 2007; 159:277–281.10.1016/j.jneumeth.2006.07.018 [PubMed: 16949675]
41. Reneer DV, Hisel RD, Hoffman JM, Kryscio RJ, Lusk BT, Geddes JW. A multi-mode shock tube for investigation of blast-induced traumatic brain injury. Journal of Neurotrauma. 2011; 28:95–104.10.1089/neu.2010.1513 [PubMed: 21083431]
42. Murphy EJ, Horrocks LA. A model for compression trauma: pressure-induced injury in cell cultures. Journal of Neurotrauma. 1993; 10(4):431–443.10.1089/neu.1993.10.431 [PubMed: 8145266]
43. Chen YC, Smith DH, Meaney DF. In-vitro approaches for studying blast-induced traumatic brain injury. Journal of Neurotrauma. 2009; 26:861–876.10.1089/neu.2008.0645 [PubMed: 19397424]
44. Prevost TP, Jin G, de Moya MA, Ala HB, Suresh S, Socrate S. Dynamic mechanical response of brain tissue in indentation in vivo, in situ and in vitro. Acta Biomaterialia. 2011; 7(12):4090–4101. http://dx.doi.org/10.1016/j.actbio.2011.06.032. 10.1016/j.actbio.2011.06.032 [PubMed: 21742064]
45. Huang B, Babcock H, Zhuang X. Breaking the diffraction barrier: super-resolution imaging of cells. Cell. 2010; 25:1047–1058.10.1016/j.cell.2010.12.002 [PubMed: 21168201]
46. Moss WC, King MJ, Blackman EG. Skull flexure from blast waves: a mechanism for brain injury with implications for helmet design. Physical Review Letters. 2009; 103(108702):1–4.10.1103/PhysRevLett.103.108702
47. Moore DF, Jérusalem A, Nyein M, Noels L, Jaffee MS, Radovitzky RA. Computational biology — modeling of primary blast effects on the central nervous system. NeuroImage. 2009; 47(2):T10–T20.10.1016/j.neuroimage.2009.02.019 [PubMed: 19248833]
48. Karen Lee KY, Nyein MK, Moore DF, Joannopoulos JD, Socrate S, Imholt T, Radovitzky R, Johnson SG. Blast-induced electromagnetic fields in the brain from bone piezoelectricity. NeuroImage. 2010; 54(S1):S30–S36. http://dx.doi.org/10.1016/j.neuroimage.2010.05.042. 10.1016/j.neuroimage.2010.05.042 [PubMed: 20547228]
49. Kamm RD, McVittie AK, Bathe M. On the role of continuum models in mechanobiology. Mechanics in Biology—ASME. 2000; 242:1–11.
50. Guilak F, Tedrow JR, Burgkart R. Viscoelastic properties of the cell nucleus. Biochemical and Biophysical Research Comunications. 2000; 269:781–786.10.1006/bbrc.2000.2360
51. Mijailovich SM, Kojic M, Zivkovic M, Fabry B, Fredberg JJ. A finite element model of cell deformation during magnetic bead twisting. Journal of Applied Physiology. 2002; 93:1429–1436.10.1152/japplphysiol.00255.2002 [PubMed: 12235044]
52. Caille N, Thoumine O, Tardy Y, Meister J-J. Contribution of the nucleus to the mechanical properties of endothelial cells. Journal of Biomechanics. 2002; 35(2):177–187.10.1016/S0021-9290(01)00201-9 [PubMed: 11784536]

53. Dao M, Lim CT, Suresh S. Mechanics of the human red blood cell deformed by optical tweezers. Journal of the Mechanics and Physics of Solids. 2003; 51:2259–2280.10.1016/j.jmps.2003.09.019
54. Karcher H, Lammerding J, Huang H, Lee RT, Kamm RD, Kaazempur-Mofrad MR. A three-dimensional viscoelastic model for cell deformation with experimental verification. Biophysical Journal. 2003; 85:3336–3349.10.1016/S0006-3495(03)74753-5 [PubMed: 14581235]
55. McGarry JG, Prendergast PJ. A three-dimensional finite element model of an adherent eukaryotic cell. European Cells and Materials. 2004; 7:27–33. [PubMed: 15095253]
56. McNally HA, Ben Borgens R. Three-dimensional imaging of living and dying neurons with atomic force microscopy. Journal of Neurocytology. 2004; 33:251–258.10.1023/B:NEUR.0000030700.48612.0b [PubMed: 15322383]
57. Jean RP, Chen CS, Spector AA. Finite-element analysis of the adhesion-cytoskeleton-nucleus mechanotransduction pathway during endothelial cell rounding: axisymmetric model. Journal of Biomechanical Engineering. 2005; 127:594–600.10.1115/1.1933997 [PubMed: 16121529]
58. Peeters AG, Oomens CWJ, Bouten CVC, Bader DL, Baaijens FPT. Viscoelastic properties of single attached cells under compression. Journal of Biomechanical Engineering. 2005; 127:237–243.10.1115/1.1865198 [PubMed: 15971701]
59. Lim, CT.; Zhou, EH.; Quek, ST. Mechanical models for living cells—a review; Journal of Biomechanics. 2006. p. 195-216.http://dx.doi.org/10.1016/j.jbiomech.2004.12.008
60. Mofrad MRK, Kamm RD. Cytoskeletal mechanics, models and measurements. Cambridge University Press. 2006
61. Vaziri A, Lee H, Mofrad MRK. Deformation of the cell nucleus under indentation: Mechanics and mechanisms. Journal of Materials Research. 2006; 21(8):2126–2135.10.1557/JMR.2006.0262
62. Lu Y-B, Franze K, Seifert G, Steinhauser C, Kirchhoff F, Wolburg H, Guck J, Janmey P, Wei E-Q, Kas J, Reichenbach A. Viscoelastic properties of individual glial cells and neurons in the CNS. PNAS. 2006; 103(47):17759–17764.10.1073/pnas.0606150103 [PubMed: 17093050]
63. Flaherty B, McGarry JP, McHugh PE. Mathematical models of cell motility. Cell Biochemistry and Biophysics. 2007; 49(1):25–28.10.1007/s12013-007-0045-2
64. Suresh S. Biomechanics and biophysics of cancer cells. Acta Biomaterialia. 2007; 3:413–438.10.1016/j.actbio.2007.04.002 [PubMed: 17540628]
65. Gladilin E, Micoulet A, Hosseini B, Rohr K, Spatz J, Eils R. 3D finite element analysis of uniaxial cell stretching: from image to insight. Physical Biology. 2007; 4(2):104–113.10.1088/1478-3975/4/2/004 [PubMed: 17664655]
66. Zhang CY, Zhang YW. Effects of membrane pre-stress and intrinsic viscoelasticity on nanoindentation of cells using AFM. Phylosophical Magazine. 2007; 87:3415–3435.10.1080/14786430701288094
67. Moreo P, García-Aznar JM, Doblaré M. Modeling mechanosensing and its effect on the migration and proliferation of adherent cells. Acta Biomaterialia. 2008; 4:613–621.10.1016/j.actbio.2007.10.014 [PubMed: 18180207]
68. Mandadapu KK, Govindjee S, Mofrad MRK. On the cytoskeleton and soft glassy rheology. Journal of Biomechanics. 2008; 41:1467–1478.10.1016/j.jbiomech.2008.02.014 [PubMed: 18402964]
69. Ingber DE. Tensegrity-based mechanosensing from macro to micro. Progress in Biophysics and Molecular Biology. 2008; 97:163–179.10.1016/j.pbiomolbio.2008.02.005 [PubMed: 18406455]
70. Zhang CY, Zhang YW. Computational analysis of adhesion force in the indentation of cells using atomic force microscopy. Physical Review E. 2008; 77:021912.10.1103/PhysRevE.77.021912
71. Ofek G, Natoli RM, Athanasiou KA. In situ mechanical properties of the chondrocyte cytoplasm and nucleus. Journal of Biomechanics. 2009; 42:873–877.10.1016/j.jbiomech.2009.01.024 [PubMed: 19261283]
72. McGarry JP. Characterization of cell mechanical properties by computational modeling of parallel plate compression. Annals of Biomedical Engineering. 2009; 37:2317–2325.10.1007/s10439-009-9772-4 [PubMed: 19680813]
73. Allena R, Mouronval A-S, Aubry D. Simulation of multiple morphogenetic movements in the drosophila embryo by a single 3D finite element model. Journal of the Mechanical Behavior of Biomedical Materials. 2010; 3(4):313–323.10.1016/j.jmbbm.2010.01.001 [PubMed: 20346899]

74. Young J, Mitran S. A numerical model of cellular blebbing: A volume-conserving, fluid–structure interaction model of the entire cell. Journal of Biomechanics. 2010; 43(2):210–220.10.1016/j.jbiomech.2009.09.025 [PubMed: 19875121]
75. Miller P, Hu L, Wang J. Finite element simulation of cell–substrate decohesion by laser-induced stress waves. Journal of the Mechanical Behavior of Biomedical Materials. 2010; 3(3):268–277.10.1016/j.jmbbm.2009.11.001 [PubMed: 20142111]
76. Bernick KB, Prevost TP, Suresh S, Socrate S. Biomechanics of single cortical neurons. Acta Biomaterialia. 2011; 7(3):1210–1219.10.1016/j.actbio.2010.10.018 [PubMed: 20971217]
77. Dintwa E, Jancsók P, Mebatsion HK, Verlinden B, Verboven P, Wang CX, Thomas CR, Tijskens E, Ramon H, Nicolaï B. A finite element model for mechanical deformation of single tomato suspension cells. Journal of Food Engineering. 2010; 103(3):265–272.10.1016/j.jfoodeng.2010.10.023
78. Yan KC, Nair K, Sun W. Three dimensional multi-scale modelling and analysis of cell damage in cell-encapsulated alginate constructs. Journal of Biomechanics. 2010; 43(6):1031–1038.10.1016/j.jbiomech.2009.12.018 [PubMed: 20096842]
79. Slomka N, Gefen A. Confocal microscopy-based three-dimensional cell-specific modeling for large deformation analyses in cellular mechanics. Journal of Biomechanics. 2010; 43:1806–1816.10.1016/j. jbiomech.2010.02.011 [PubMed: 20188374]
80. Dao M, Li J, Suresh S. Molecularly based analysis of deformation of spectrin network and human erythrocyte. Materials Science and Engineering C. 2006; 26:1232–1244.10.1016/j.msec.2005.08.020
81. Li J, Lykotrafitis G, Dao M, Suresh S. Cytoskeletal dynamics of human erythrocyte. PNAS. 2007; 104:4937–4942.10.1073/pnas.0700257104 [PubMed: 17360346]
82. Quinn DJ, Pivkin I, Wong SY, Chiam K-H, Dao M, Karniadakis GE, Suresh S. Combined simulation and experimental study of large deformation of red blood cells in microfluidic systems. Annals of Biomedical Engineering. 2011; 39:1041–1050.10.1007/s10439-010-0232-y [PubMed: 21240637]
83. Diez-Silva M, Dao M, Han J, Lim C-T, Suresh S. Shape and biomechanical characteristics of human red blood cells in health and disease. MRS Bulletin. 2010; 35:382–388.10.1557/mrs2010.571 [PubMed: 21151848]
84. Kaplus M, Kuriyan J. Molecular dynamics and protein function. PNAS. 2005; 102(19):6679–6685.10.1073/pnas.0408930102 [PubMed: 15870208]
85. Ayton GS, Voth GA. Multiscale simulation of protein mediated membrane remodeling. Seminars in Cell and Developmental Biology. 2010; 21(4):357–362.10.1016/j.semcdb.2009.11.011 [PubMed: 19922811]
86. Deriu MA, Bidone TC, Mastrangelo F, Di Benedetto G, Soncini M, Montevecchi FM, Morbiducci U. Biomechanics of actin filaments: A computational multi-level study. Journal of Biomechanics. In Press. 10.1016/j.jbiomech.2010.11.014
87. Hu L, Zhang X, Miller P, Ozkan M, Ozkan C, Wang J. Cell adhesion measurement by laser-induced stress waves. Journal of Applied Physics. 2006; 100(084701):1–5.10.1063/1.2356107
88. Holzapfel, GA. Nonlinear Solid Mechanics. John Wiley & Sons; 2000.
89. Taylor RL, Pister KS, Goudreau GL. Thermomechanical analysis of viscoelastic solids. International Journal for Numerical Methods in Engineering. 1970; 2(1):45–59.10.1002/nme.1620020106
90. Kaliske M, Rothert H. Formulation and implementation of three-dimensional viscoelasticity at small and finite strains. Computational Mechanics. 1997; 19(3):228–239.10.1007/s004660050171
91. Meyers, Marc A. Dynamic behavior of materials. Wiley Interscience; 1994.
92. Drumheller DS. Introduction to wave propagation in nonlinear fluids and solids. Cambridge University Press. 1998
93. Conde C, Cáceres A. Microtubule assembly, organization and dynamics in axons and dendrites. Nature Reviews Neuroscience. 2009; 10:319–332.10.1038/nrn2631
94. Simulia, Abaqus 6.10. 2010
95. Alley, Matthew David. Master's thesis. Purdue University; 2009. Explosive blast loading experiments for TBI scenarios: characterization and mitigation.

96. Sondén A, Svensson B, Roman N, Ostmark H, Brismar B, Palmblad J, Kjellström BT. Laser-induced shock wave endothelial cell injury. Lasers in Surgery and Medicine. 2000; 26:364–375.10.1002/(SICI)1096-9101(2000)26:4 [PubMed: 10805941]

97. Guilak F. Compression-induced changes in the shape and volume of the chondrocyte nucleus. Journal of Biomechanics. 1995; 28:1529–1541.10.1016/0021-9290(95)00100-X [PubMed: 8666592]

98. Nagayama K, Mori Y, Shimada K. Shock Hugoniot compression curve for water up to 1 GPa by using a compressed gas gun. Journal of Applied Physics. 2002; 91(1):476–482.10.1063/1.1421630

99. Boehler R, Kennedy G. Pressure dependence of the thermodynamical grüneisen parameters of fluids. Journal of Applied Physics. 1977; 48(10):4183–4186.

100. Barron THK, White GK. Heat capacity and thermal expansion at low temperatures. Kluwer Academic/Plenu. 1999

101. Bett KE, Cappi JB. Effect of pressure on the viscosity of water. Nature. 1965; 207:620–621.10.1038/207620a0

102. Nagayama K, Mori Y, Motegi Y, Nakahara K. Shock Hugoniot for biological materials. Shock Waves. 2006; 15:267–275.10. 1007/s00193-006-0030-5

103. Salvador-Silva M, Aoi S, Parker A, Yang P, Pecen P, Hernandez MR. Responses and signaling pathways in human optic nerve head astrocytes exposed to hydrostatic pressure in vitro. Glia. 2003; 45(4):364–377.10.1002/glia.10342 [PubMed: 14966868]

104. Stricker J, Falzone T, Gardel ML. Mechanics of the F-actin cytoskeleton. Journal of Biomechanics. 2010; 43(1):9–14.10.1016/j.jbiomech.2009.09.003 [PubMed: 19913792]

105. McCall K. Genetic control of necrosis—another type of programmed cell death. Current Opinion in Cell Biology. 2010; 22(6):882–888.10.1016/j.ceb.2010.09.002 [PubMed: 20889324]

106. Challa S, Ka-Ming Chan F. Going up in flames: necrotic cell injury and inflammatory diseases. Cellular and Molecular Life Sciences. 2000; 67(19):3241–3253.10.1007/s00018-010-0413-8 [PubMed: 20532807]

107. Christofferson DE, Yuan J. Necroptosis as an alternative form of programmed cell death. Current Opinion in Cell Biology. 2010; 22(2):263–268.10.1016/j.ceb.2009.12.003 [PubMed: 20045303]

108. Shi R, Whitebone J. Conduction deficits and membrane disruption of spinal cord axons as a function of magnitude and rate of strain. Journal of Neurophysiology. 2006; 95(6):3384–3390.10.1152/jn.00350.2005 [PubMed: 16510778]

109. Suzuki H, Kumai T, Matsuzaki M. Effect of temperature decline on the cytoskeletal organization of the porcine oocyte. Journal of Mammalian Ova Research. 2007; 24:107–113.10.1274/jmor.24.107

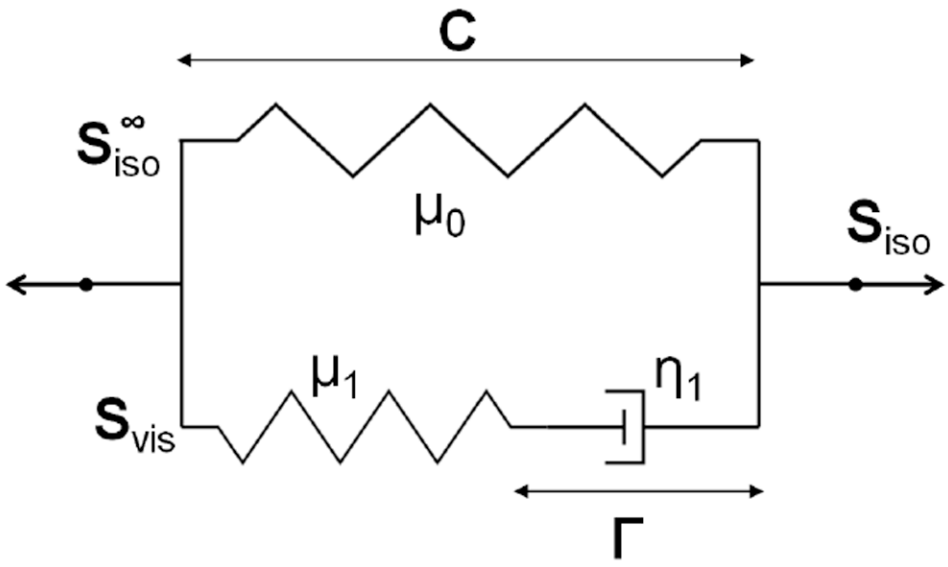

Figure 1.
First order generalized Maxwell model

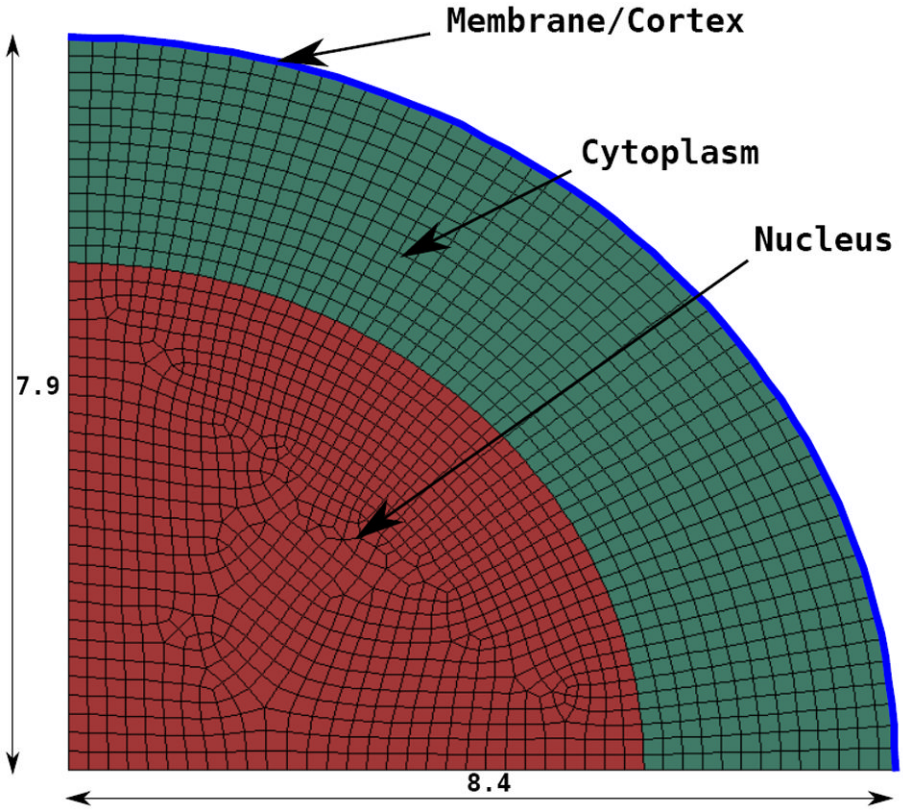

Figure 2.
2D axisymmetric mesh of the neuron used for nanoindentation (distances in μm)

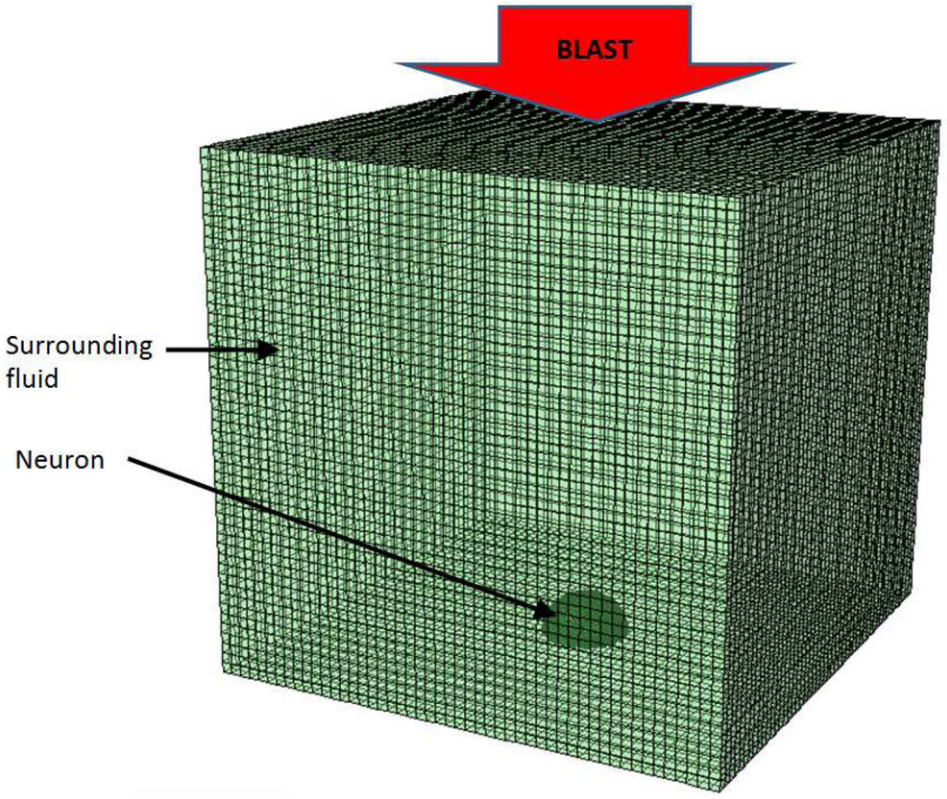

Figure 3.
Finite element setup of the blast simulation

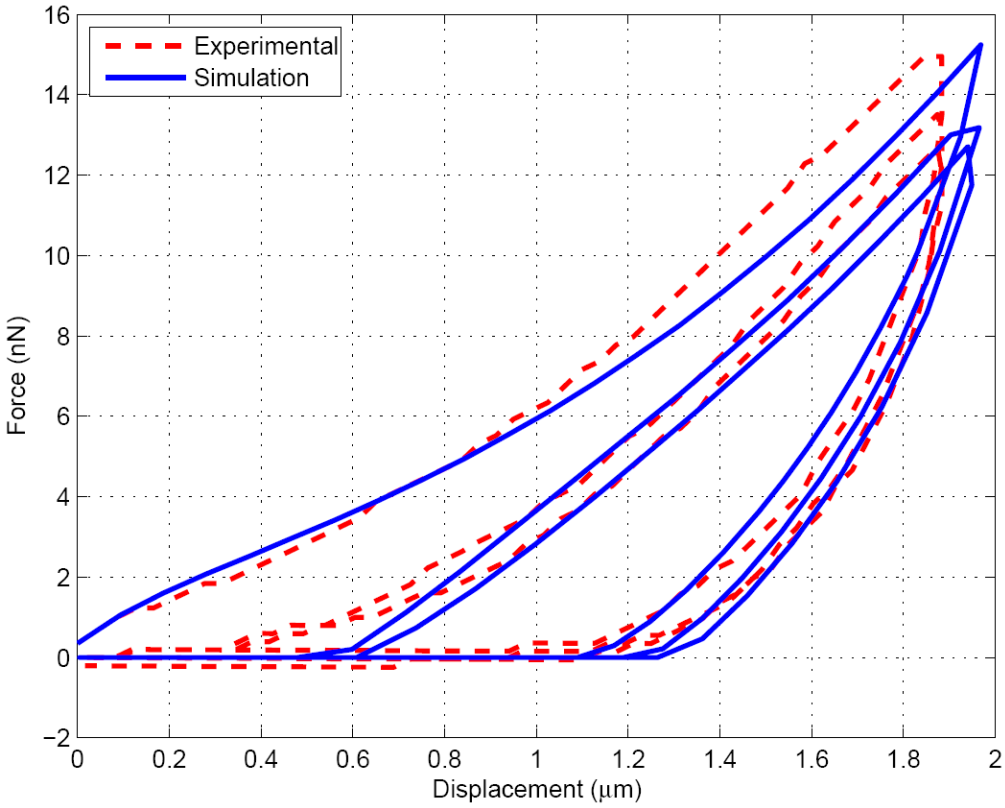

Figure 4.
Indentation force v.s. displacement for the fast cycle ($10\mu m.s^{-1}$)

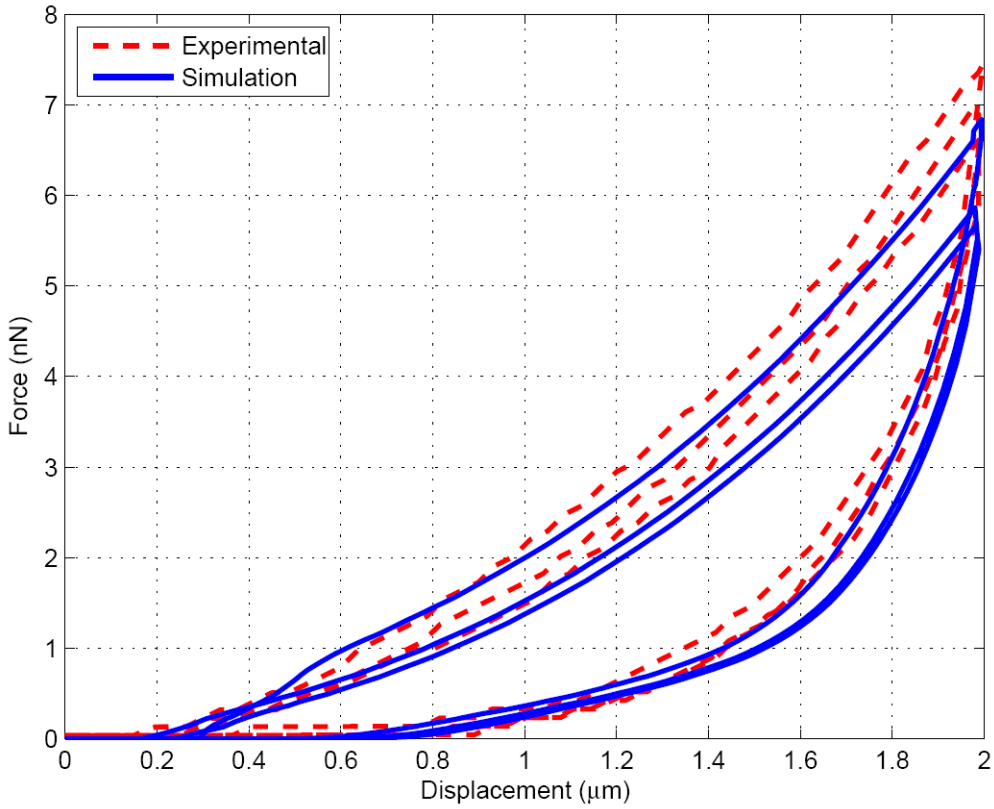

Figure 5.
Indentation force v.s. displacement for the medium cycle ($1\mu m.s^{-1}$)

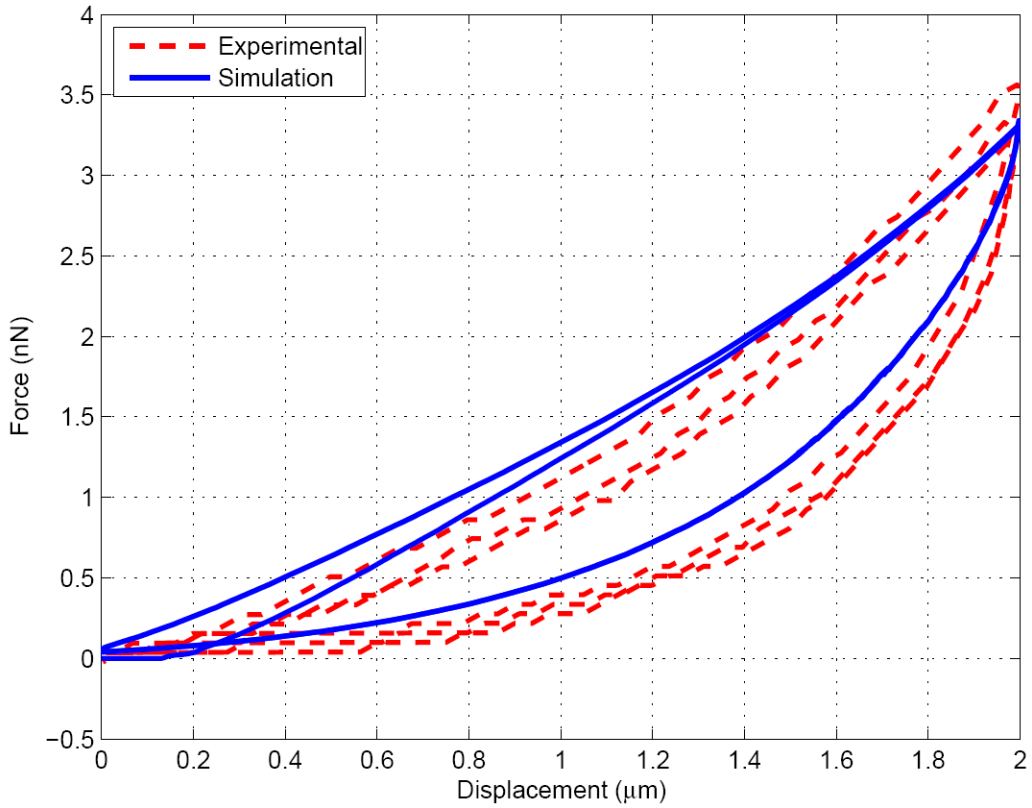

Figure 6.
Indentation force v.s. displacement for the slow cycle ($0.1\mu m.s^{-1}$)

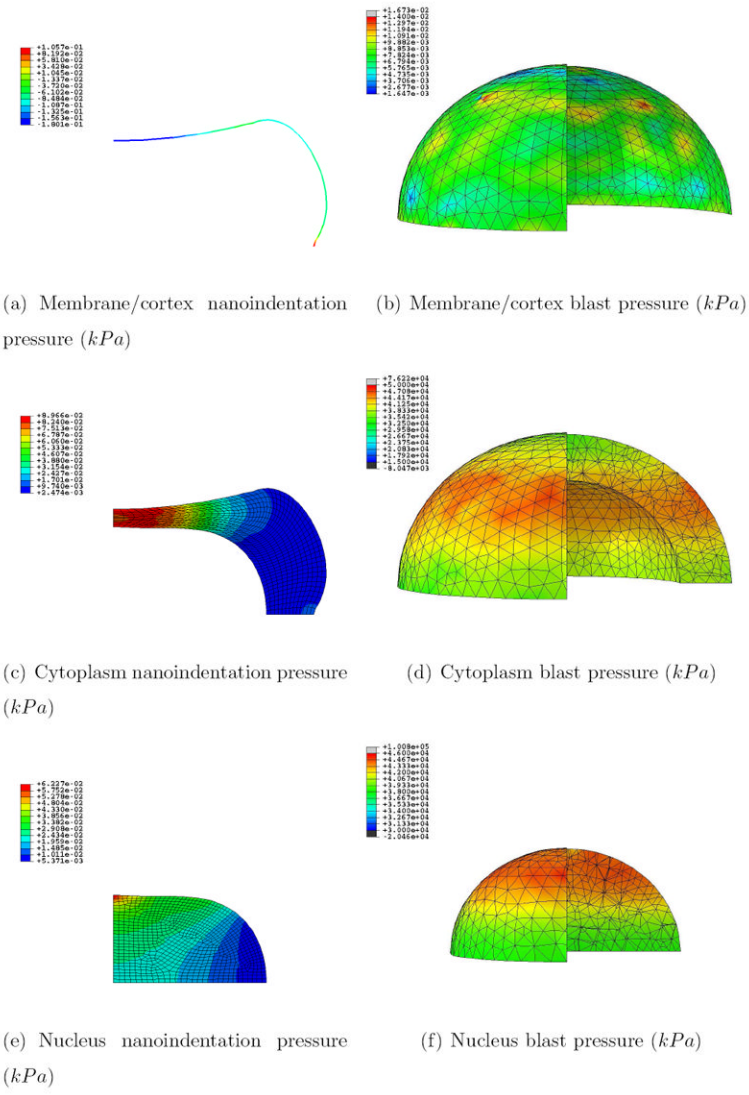

(a) Membrane/cortex nanoindentation pressure (kPa)

(b) Membrane/cortex blast pressure (kPa)

(c) Cytoplasm nanoindentation pressure (kPa)

(d) Cytoplasm blast pressure (kPa)

(e) Nucleus nanoindentation pressure (kPa)

(f) Nucleus blast pressure (kPa)

Figure 7.
Pressure field (*kPa*) for the nanoidentation and blast simulations at 26.88 *s* and 65.5 *ns* respectively for the three regions; a quarter of the mesh for the blast simulation was taken out for visualization purposes

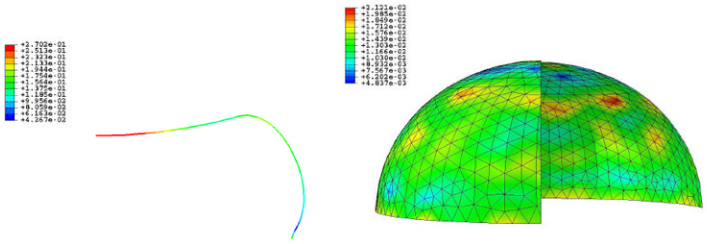

(a) Membrane/cortex nanoindentation von Mises stress (kPa)

(b) Membrane/cortex blast von Mises stress (kPa)

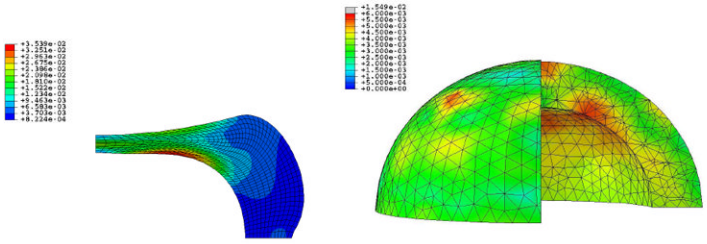

(c) Cytoplasm nanoindentation von Mises stress (kPa)

(d) Cytoplasm blast von Mises stress (kPa)

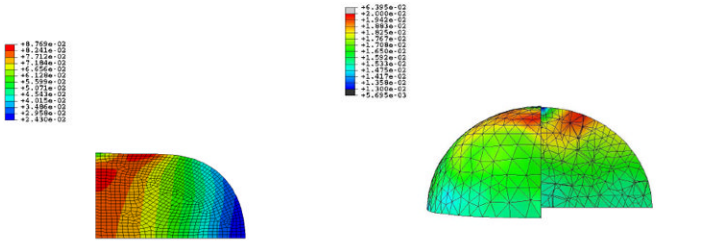

(e) Nucleus nanoindentation von Mises stress (kPa)

(f) Nucleus blast von Mises stress (kPa)

Figure 8.

Von Mises stress field (*kPa*) for the nanoidentation and blast simulations at 26.88 *s* and 65.5 *ns* respectively for the three regions; a quarter of the mesh for the blast simulation was taken out for visualization purposes

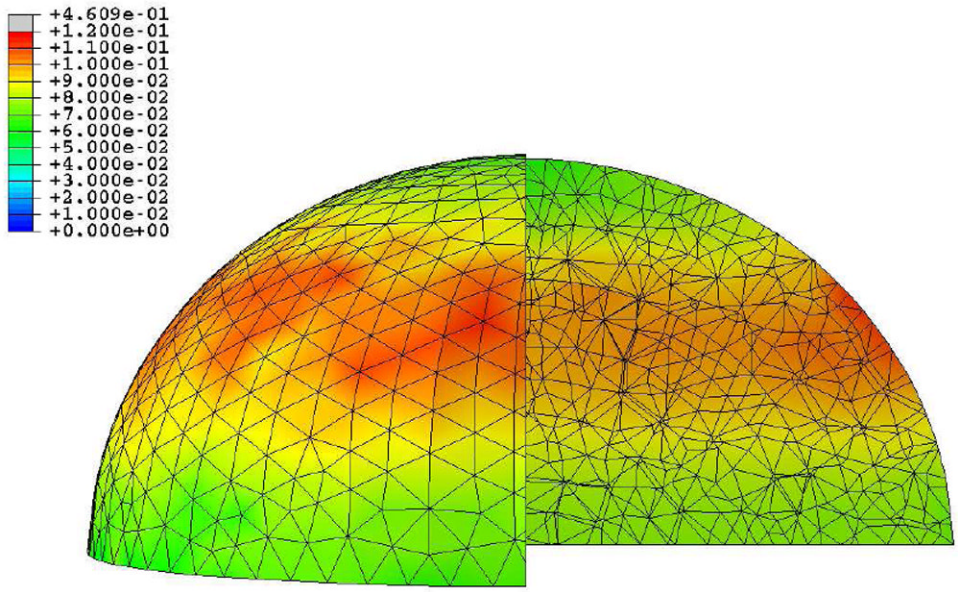

Figure 9.
Temperature increase field (*K*) for the blast simulation at 65.5 *ns* for the whole cell; a quarter of the mesh was taken out for visualization purposes

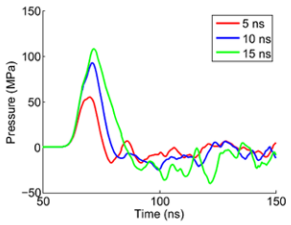

(a) Pressure evolution (MPa)

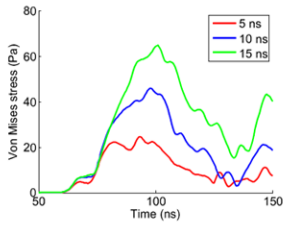

(b) Von Mises stress evolution (Pa)

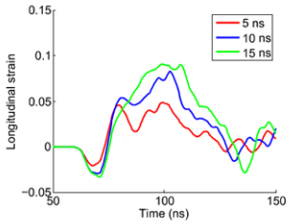

(c) Longitudinal strain evolution

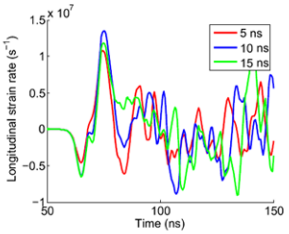

(d) Longitudinal strain-rate evolution (s^{-1})

Figure 10.
Pressure, von Mises stress, longitudinal strain and strain-rate evolution at the nucleus-cytoplasm interface, and ~75 % of the nucleus height, for three initial positive phase durations: 5, 10 and 15 *ns*

Table 1

Nanoindentation loading cycles followed by Bernick *et al.* [76] (rates are given in $\mu m.s^{-1}$; "0", "+" and "-" represent a plateau, loading and unloading respectively between the initial indentation depth δ_0 at Steps A and B to $\delta_0 + 2\mu m$)

Cycles	**A**	**B**	C_1						C_2						C_3						**D**	**E**
Load	+	0	+	-	+	-	+	-	+	-	+	-	+	-	+	-	+	-	+	-	+	0
Rate	0.3	0	10						1						0.1						10	0

Table 2

Model parameters

δ_0		c_0^{mem}	d_0^{mem}	μ_1^{mem}	τ_1^{mem}	c_0^{cyto}
1.41 μm		166.67 Pa	0 Pa^{-1}	13.89 Pa	3000 s	1.67 Pa
d_0^{cyto}	μ_1^{cyto}	τ_1^{cyto}	c_0^{nuc}	d_0^{nuc}	μ_1^{nuc}	τ_1^{nuc}
0 Pa^{-1}	107.78 Pa	0.01 s	13.33 Pa	0 Pa^{-1}	862.22 Pa	0.5 s

Table 3

Comparison between the maximum forces of an indentation experiment [76] (Exp) and simulation (Sim) for a specific representative cell; $C_{\alpha,\beta}$ refers to cycle α, maximum loading β (see Table 2)

Cycles	$C_{1,i}$	$C_{1,ii}$	$C_{1,iii}$	$C_{2,i}$	$C_{2,ii}$	$C_{2,iii}$	$C_{3,i}$	$C_{3,ii}$	$C_{3,iii}$
Exp (*nN*)	11.5	10.8	10.3	5	4.9	4.8	3	3	3
Sim (*nN*)	11.5	11	10.2	5.3	4.6	4.3	2.5	2.5	2.5
Error	0%	2%	1%	6%	6%	1%	17%	17%	17%

Acta Biomater. Author manuscript; available in PMC 2013 September 01.